Radiation Measurements 177 (2024) 107253

Contents lists available at ScienceDirect

Radiation Measurements

journal homepage: www.elsevier.com/locate/radmeas

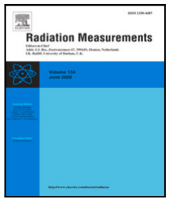

Computational design and evaluation of a quad-MOSFET device for quality control of therapeutic accelerator-based neutron beams

Klaudiusz Jakubowski [a,c], James Vohradsky [a], Andrew Chacon [c], Daniel R. Franklin [b], Linh T. Tran [a], Susanna Guatelli [a], Mitra Safavi-Naeini [c,a], Anatoly Rosenfeld [a,*]

[a] Centre for Medical Radiation Physics, University of Wollongong, Australia
[b] School of Electrical and Data Engineering, University of Technology Sydney, Australia
[c] Australian Nuclear Science and Technology Organisation, Australia

ARTICLE INFO

Keywords:
BNCT
Neutron capture
QC
Dosimetry
MOSFET
Particle accelerators

ABSTRACT

Accurate real-time monitoring of neutron beams and distinguishing between thermal, epithermal and fast neutron components in the presence of a photon background is crucial for the effectiveness of accelerator-based boron neutron capture therapy (AB-BNCT). In this work, we propose an innovative quadruple metal–oxide–semiconductor field-effect transistor (MOSFET) device for real-time, cost-effective beam quality control; one detector is kept uncovered while the other three are covered with either a B_4C, cadmium and B_4C or polyethylene converter.

Individual MOSFET converter configurations were optimised via Monte Carlo simulations to maximise signal selectivity across neutron energy spectra. Results demonstrate the quad-MOSFET device's efficacy in quantifying changes in neutron flux, underscoring its potential as a useful instrument in the AB-BNCT quality control process.

1. Introduction

With the development of accelerator-based (AB) neutron sources, there has been a renewed interest in boron neutron capture therapy (BNCT) as a cancer treatment modality, notably for glioblastoma multiforme, head and neck cancer, melanoma and malignant mesothelioma (Dymova et al., 2020; Barth et al., 2018; Malouff et al., 2021). As of 2022, there are a total of 26 AB-BNCT projects worldwide (ISNCT, 2022; Kiyanagi et al., 2019; Suzuki, 2019). These include nine clinical facilities, seven dedicated to experimental use, five in the commissioning phase and five in the construction or development stages. BNCT utilises the thermal neutron capture reaction in ^{10}B, delivered to cancer cells by targeted agents such as boronophenylalanine (^{10}B-BPA) and sodium mercaptoundecahydro-closo-dodecaborate (^{10}B-BSH) (Futamura et al., 2017). Each ^{10}B neutron capture reaction releases a high linear energy transfer (LET) α particle and ^{7}Li ion, which, due to their short range in tissue, deliver a high dose directly to tumour cells.

BNCT uses epithermal neutrons to treat deep-seated tumours, since these neutrons will thermalise within the patient before reaching the target. Although ^{10}B is selectively delivered to the target, it also accumulates in skin cells and surrounding tissues. Therefore, a neutron beam with a substantial thermal neutron component increases the skin (or entrance) dose for a given target dose compared to a beam spectrum dominated by epithermal neutrons. For example, Hu et al. (2021) modelled AB-BNCT treatments using the NeuCure and SERA treatment planning systems (TPS) and independent PHITS Monte Carlo simulations, reporting maximum skin doses of around 3.0–4.4 Gy, 2.1 Gy, 0.2–0.5 Gy, and 1.6–1.8 Gy due to boron, gamma, nitrogen and hydrogen dose components, respectively. Current beam monitoring in AB-BNCT primarily evaluates physical figures of merit for the in-air neutron beam as defined by the IAEA, including the absolute epithermal neutron flux, the thermal to epithermal neutron flux ratio, the fast neutron and gamma dose rates to epithermal neutron flux ratios, and the total net neutron flux to epithermal flux ratio (IAEA, 2001).

This study aims to develop a real-time quality control (QC) device for AB-BNCT treatment validation by monitoring the incident neutron beam properties throughout irradiation. The ideal detector for this purpose would be compact, low-cost, and provide real-time readouts of the proportions of thermal, epithermal and fast neutron as well as γ flux or fluence, independently of the dose rate. To date, no commercially available device meets all these criteria. Passive detectors, such as luminescence dosimeters (thermoluminescent dosimeters (TLDs) and optically stimulated luminescent dosimeters (OSLDs)), radiochromic films or solid state nuclear track detectors (SSNTD) cannot be read

* Correspondence to: School of Physics, University of Wollongong, NSW 2522, Australia.
E-mail address: anatoly@uow.edu.au (A. Rosenfeld).

https://doi.org/10.1016/j.radmeas.2024.107253
Received 23 February 2024; Received in revised form 19 July 2024; Accepted 22 July 2024
Available online 24 July 2024

in real-time; their signal is averaged over the duration of the measurement, and it is not possible to detect short-term fluctuations in beam flux. These detectors also usually require long pre- or post-irradiation preparation and specific equipment, and their sensitivity can be dependent on LET, resulting in a decrease in response with increasing ionisation density (Jong et al., 2014; Costa et al., 2010; Olko, 2010; Santos et al., 2021; Devic et al., 2019; Ogawara et al., 2020; Ambrozova et al., 2017). Small volume ion chambers operate in an active mode, but suffer from volume averaging and stem effect (Kweon et al., 2011; de Prez et al., 2019). Other real-time detectors have been proposed, such as PN diodes (Takada et al., 2021) or a scintillator combined with a quartz fibre (Tanaka et al., 2018), but none of these devices can simultaneously measure the individual components of the beam.

We propose a novel application of metal-oxide semiconductor field-effect transistors (MOSFETs) for real time neutron beam quality control. MOSFETs are solid-state devices whose threshold voltage V_{th}[1] increases almost linearly with the accumulated ionising radiation dose, due to the creation of permanent charge dislocations (i.e., trapped holes) in the gate oxide-silicon interface. The sensitivity of a MOSFET dosimeter can be adjusted by controlling the gate bias or the thickness of the oxide layer, and the device can compensate for the temperature-dependence of V_{th} by using an integrated PN junction as a temperature sensor (Rosenfeld et al., 2011). In summary, MOSFETs are a flexible and precise candidate for real-time radiation dosimetry. By modulating a MOSFET detector's response to radiation of different types and energy ranges through the addition of layers of different materials (converters), the dose measured by the MOSFET can be used to indirectly estimate other properties of the radiation field (Kaplan et al., 1999).

The design of our system is based on an optimised combination of four MOSFET detectors for real-time measurement of the relative thermal, epithermal and fast neutron flux and the flux of the γ radiation in high-intensity mixed gamma/neutron fields. The MOSFETs were optimised by simulating a range of converter thicknesses and selecting those that provided optimal selectivity and sensitivity for the thermal, epithermal and fast neutron components. The performance of the optimised quad-MOSFET device was then evaluated for two operational scenarios: first, as a quality control device used in free air, for checking beam quality; and second, as a real-time beam-monitoring device placed on the patient's skin and used throughout beam delivery and patient treatment where the impact of backscatter on its performance was assessed. The final design was then evaluated using Geant4 in a realistic accelerator-based neutron radiation field to determine the ability of the device to estimate the relative change in flux recorded by each device.

The remainder of this paper is organised as follows. The simulation parameters and MOSFET detector configuration, as well as the methods to optimise its design and study the response and sensitivity of the detectors, are explained in Section 2. Simulation results are presented and discussed in Section 3; the final conclusions from our work are presented in Section 4.

2. Materials and methods

2.1. Simulation configuration

Utilising Geant4 (version 11.1, patch 01), simulations were performed to model the neutron interactions with the detectors (Agostinelli et al., 2003; Allison et al., 2006, 2016; García et al., 2013; Thulliez et al., 2022). A complete list of the physics models used in this work is presented in Table S1 in the Supplementary Material; this list was validated experimentally in our previous work (Jakubowski et al., 2023). The models included in the list have also been used in other studies using neutron beams (Vohradsky et al., 2019, 2021; Lamrabet et al., 2021), and have also been compared to the well-known Monte Carlo N-Particle Transport Code (MCNP) simulation framework, and shown to be in good agreement (van der Ende et al., 2016; Hartling et al., 2018).

2.2. MOSFET detector and converter configuration

The proposed device consists of four MOSFET detectors — three that are sensitive to neutrons of specific energy bands via different converter layers, and a fourth that is used to correct for dose components common to all four devices due to radiation which directly interacts with the sensitive volume. The manufacturing process is able to ensure that the thickness of the physical sensitive volume in the MOSFET detector is within 1% of the nominal value, providing a high degree of consistency between the response of individual devices. Thermal and epithermal neutron fluence is estimated using a MOSFET detector coupled with a boron carbide (B_4C) converter, which captures neutrons and releases α and ^{7}Li particles (Kaplan et al., 1999; Fragopoulou et al., 2010; Vohradsky et al., 2019). By placing an additional (natural) cadmium layer, which exhibits a very high thermal neutron capture cross section, on top of the B_4C converter on a second MOSFET, device response is limited to the epithermal neutron energy band. A MOSFET with a polyethylene (PE) layer is used to indirectly measure fast neutron fluence via recoiled protons due to the ^{1}H(n,p)^{1}H reaction. Finally, a correction factor is obtained using a fourth detector, which provides information about the radiation field components directly interacting with the sensitive volume (SV), including the γ radiation and inelastic neutron reactions in the gate oxide layer (i.e., Si(n, α) reactions). The epithermal component of the neutron beam can also interact with nitrogen in the air, generating 0.584 MeV recoil protons from the ^{14}N(n, p)^{14}C reaction. These protons are blocked by the B_4C and polyethylene layers on top of the respective MOSFETS; an additional aluminium shielding layer performs this function on the bare detector.

The MOSFET detector models are shown in Fig. 1(b). Each MOSFET detector comprises a 350 μm thick silicon substrate, a silicon dioxide SV with an area of 0.6 mm × 0.8 mm and a thickness of 1 μm, a 1 μm thick aluminium layer (gate contact), and a converter layer. The MOSFET detector with the B_4C converter is manufactured with an additional aluminium support layer for increased mechanical stability. The area of the PE converter is 1 mm × 1.2 mm, which is larger than the MOSFET's gate area in order to increase the number of recoil protons incident on the SV. All evaluated converters and aluminium layers are summarised in Table 1, and the models for all MOSFET and converter combinations are shown in Figs. 1(c) and 1(f).

2.3. Spectral selectivity and converter optimisation

First, the converter geometries were simulated (three B_4C, three Cd + B_4C and eight PE layer thicknesses) along with the bare MOSFET. A 1 cm circular neutron beam, replicating the University of Tsukuba Hospital iBNCT epithermal neutron spectrum (Fig. 2), was emitted towards the detector from a distance of 5 cm in all simulations (Kumada et al., 2018).

The number of primary particles was determined by running a batch of 10 simulations with different random seeds for the MOSFET with the PE converter, calculating the mean and standard deviation of the total energy deposition in the SV across the 10 runs, and then exponentially increasing the number of primary particles until the ratio of σ/μ converges (i.e., changes by less than 5% with a doubling of the number of primary particles).[2] The convergence criterion was satisfied

[1] V_{th} is the minimum gate voltage required to establish a source–drain conduction channel in a MOSFET.

[2] The MOSFET + PE converter was used for this process, since this is the least-sensitive detector/converter combination.

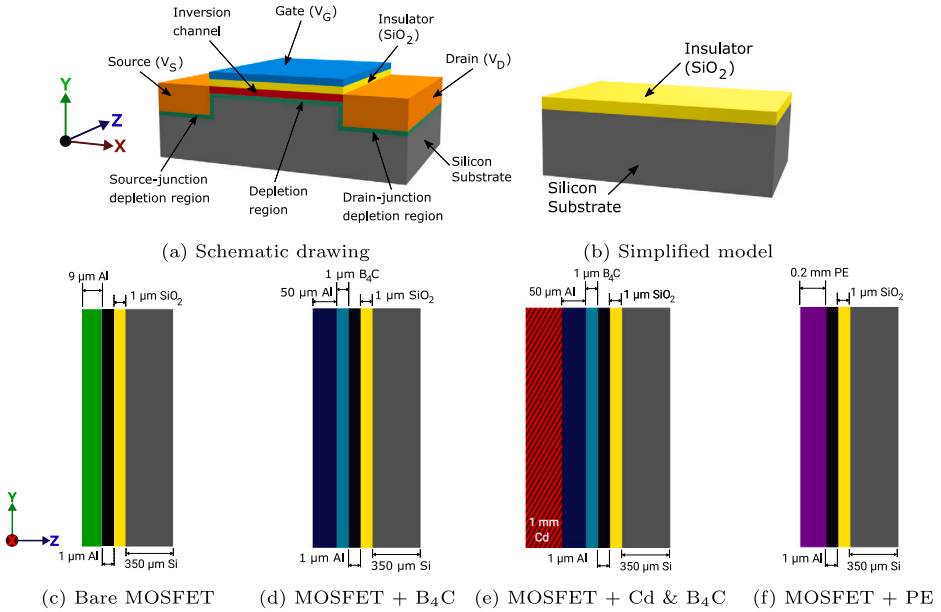

Fig. 1. Schematic illustrating the internal structure of a MOSFET detector, together with the simplified structures used in the simulations. Cross-sections of each of the three MOSFETs used in this study are shown with their respective converters and shields/support layers; the silicon substrate is shown in grey, the sensitive volume (SiO_2) in yellow and the aluminium gate contact layers in black; the aluminium shield on the bare detector is shown in green, the B_4C converter in cyan with the aluminium layer on the top in dark blue, cadmium filter in red, and the PE converter is shown in violet.

Table 1
Simulated MOSFET converter materials, densities, compositions and thicknesses.

Converter	Density (g/cm^3)	Mass composition	Evaluated thicknesses (μm)
B_4C	2.45	75.9% ^{10}B, 17.0% C, 3.8% Mg, 2.4% ^{11}B, 0.6% O and 0.3% H	1, 2, 3
Cd	8.65	100.0% Cd	500, 750, 1000
Al support layer	2.70	100.0% Al	0, 50
PE ($(C_2H_4)_n$)	0.94	86.0% C, 14.0% H	10, 50, 100, 200, 1000, 3000, 5000, 6000
Al shield	2.70	100.0% Al	0, 9

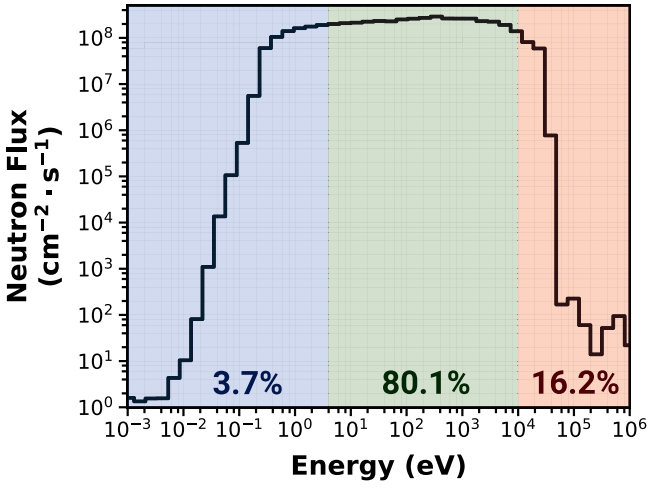

Fig. 2. iBNCT neutron energy spectrum (data courtesy of Kumada et al. (2018)) used in this study, highlighted to illustrate the three neutron energy windows as defined by the IAEA: $E_{thermal} < 0.4$ eV (blue), 0.4 eV $< E_{epithermal} < 10$ keV (green), and $E_{fast} > 10$ keV (IAEA, 2001) (red). The proportion of neutrons within each energy window in the input neutron spectrum is 3.7%, 80.1% and 16.2%, respectively.

with 10^9 primary particles, resulting in a total neutron fluence at the detector surface of 1.27×10^{11} cm^{-2}.

Next, batches of 10 simulations were performed with 10^9 primary particles in which (1) the kinetic energy of all particles incident on the SV surface, and (2) energy deposition within the SV of the MOSFET were scored and plotted as a function of particle energy. The spectrum of energy deposition events recorded in the SV, the identity of the contributing particles (secondary charged particles, gamma and inelastic interactions with neutrons) and the total deposited dose were recorded. The spectra were analysed to define a threshold that separates the energy deposition of secondary particles of interest to the energy deposited by all other particles. In the case of the B_4C and Cd + B_4C converters, this corresponds to the charge deposited by the α particles and ^{7}Li ions, whereas for the PE converters, it represents the contribution of the recoil protons. The spectral selectivity ratio (SSR), defined as the total energy deposited above this threshold to the total energy deposited below the threshold is the primary figure of merit (FOM) used in this work.

The best-performing B_4C converter was simulated with an additional 50 μm supporting aluminium layer for mechanical stability, and its impact on its spectral selectivity was evaluated. Finally, a 9 μm aluminium shield was added on top of the bare MOSFET to confirm its utility for blocking recoil protons generated in air (external to the SV) without altering the recorded neutron spectrum.

2.4. Response characterisation of the optimal configuration of MOSFET detectors

Two configurations were simulated in which the quad-MOSFET device was placed at a distance of 5 cm from the neutron source: in the first, the device was simulated in air, while in the second, the device was placed against a water phantom (Fig. 3). For each configuration,

Table 2
Spectral selectivity ratios, ground truth dose (D_{GT}) defined as dose deposited in the SV of the converter-covered MOSFETs by particles of interest, estimated dose (D_{est}) calculated by subtracting energy deposition in the bare MOSFET SV from total deposited dose in converter-covered MOSFETs, and percentage difference between D_{est} and D_{GT}.

Layer	Thickness (μm)	SSR	D_{GT} (Gy)	D_{est} (Gy)	$\frac{D_{est}-D_{GT}}{D_{GT}}$ (%)
B_4C	1	1.6	1.9×10^{-10}	1.9×10^{-10}	0.0
	2	1.3	2.3×10^{-10}	2.3×10^{-10}	0.0
	3	1.0	2.3×10^{-10}	2.3×10^{-10}	0.0
Cd+B_4C	0.5	1.0	1.3×10^{-10}	1.3×10^{-10}	0.0
	0.75	1.1	1.3×10^{-10}	1.3×10^{-10}	0.0
	1	1.1	1.2×10^{-10}	1.2×10^{-10}	0.0
PE	10	2.3	1.6×10^{-13}	1.7×10^{-13}	4.8
	50	2.8	2.3×10^{-13}	2.4×10^{-13}	5.8
	100	2.9	2.4×10^{-13}	2.5×10^{-13}	6.2
	200	3.0	2.4×10^{-13}	2.6×10^{-13}	5.4
	1000	3.2	2.4×10^{-13}	2.5×10^{-13}	5.3
	3000	3.7	2.2×10^{-13}	2.3×10^{-13}	3.6
	5000	4.7	2.1×10^{-13}	2.1×10^{-13}	0.9
	6000	5.1	1.9×10^{-13}	1.8×10^{-13}	−1.7

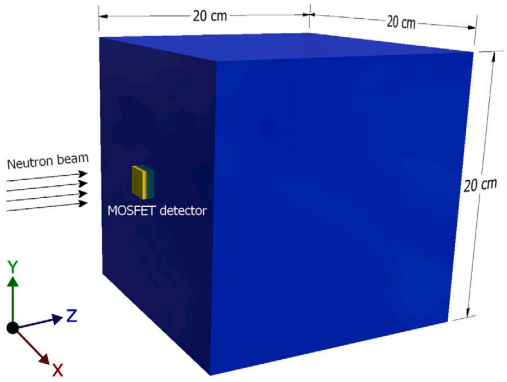

Fig. 3. Schematics of the simulation configuration of the MOSFET device placed on the surface of the water phantom; this configuration was used to determine the contribution of backscatter to the device.

the doses deposited in the SV of each detector by individual secondary particles, as well as the percentage of secondary particles generated due to the $^{10}B(n, \alpha)^7Li$ and $^1H(n, p)^1H$ reactions, were scored.

The response of the B_4C, Cd + B_4C and PE-coated MOSFET detectors has been further evaluated as a function of the incident neutron energy. The detectors were exposed to fourteen monoenergetic beams of 1×10^9 neutrons, with energies ranging from 1×10^{-3} eV to 5 MeV. The detection efficiency is defined as:

$$\epsilon = \frac{counts}{\Phi} \times 100\% \quad (1)$$

where "**counts**" refers to the number of secondary particles of interest registered in the SV of individual MOSFET detectors. These secondary particles include α particles from $^{10}B(n, \alpha)^7Li$ reactions and elastically scattered protons from $^1H(n, p)^1H$ reactions on PE; Φ represents the fluence of the primary neutrons incident on the detector.

2.5. Sensitivity of the MOSFET detectors

Finally, we investigated the sensitivity of the B_4C, Cd + B_4C and PE-coated MOSFET detectors to the thermal, epithermal and fast neutron energy regions of the Tsukuba University Hospital neutron spectrum. The average neutron flux used in clinical AB-BNCT is in the order of 10^9 n/cm^2/s. Therefore, we studied the sensitivity of the quad-MOSFET device to small changes in neutron fluence using 9×10^8, 1×10^9 and 1.1×10^9 neutrons and by calculating percentage differences in the deposited doses. Additionally, we evaluated the thermal to epithermal and fast to epithermal neutron ratios. This involved comparing the doses delivered to the SV of the MOSFET detectors covered with B_4C and Cd + B_4C, and PE and Cd + B_4C after subtraction of the bare MOSFET signal for the three fluence conditions.

3. Results and discussion

3.1. Optimisation of the detector design

The spectra of the dominant species of secondary particles scored in the SV of the B_4C, Cd + B_4C and PE-covered MOSFETs are shown in Fig. 4. Based on these spectra, the energy threshold E_{th} used for the calculation of the SSR is defined as 10 keV. For the B_4C and Cd + B_4C converter (Fig. 4(b)), the spectrum above 10 keV is dominated by the α particles and ^7Li products of the ^{10}B neutron capture reaction, while for PE the spectrum above 10 keV is dominated by the recoil protons (see Fig. 4(d)).[3]

The kinetic energy spectra of the secondary particles as they enter the SV of the bare (no converter) MOSFET detector (with and without a 9 μm aluminium layer) and the corresponding energy deposition spectra (in the MOSFET SVs) are shown in Figs. 5(a) and 6(a). Equivalent spectra (particle kinetic energy and energy deposition) for the MOSFETs covered with 1 μm, 2 μm and 3 μm B_4C converters are shown in Figs. 5(b) and 6(b); and MOSFETs covered with 1 μm B_4C and 0.5 mm, 0.75 mm and 1 mm Cd in Figs. 5(c) and 6(c). Finally, spectra for MOSFETs covered with 0.01–6 mm thick PE converter layers are shown in Figs. 5(d) and 6(d).

Table 2 lists the spectral selectivity ratios, normalised dose deposited in the detector's SV resulting from the neutron capture reaction of interest, and the difference between this dose and the dose to the bare detector (expressed as a percentage) for the MOSFETs with the B_4C, Cd + B_4C and PE converter layers of each evaluated thickness.

Energy deposition in the bare (no converter) MOSFET with the 9 μm aluminium layer decreases by up to 40% at energies of around 70–400 keV compared to the MOSFET without the aluminium layer. However, the total dose deposited across the entire spectrum is approximately 90% of that deposited in the completely bare MOSFET (see Supplementary Materials, Table S2). The additional 9 μm aluminium layer is sufficient to stop protons from the $^{14}N(n,p)^{14}C$ reaction, which are also naturally blocked by the B_4C (and Cd), Al substrate layers and PE converter. Neutrons can activate the aluminium layer and generate a small number of γ-rays; however, they deposit a negligible amount of energy in the 1 μm thick silicon dioxide SV. The increase in the flux of 1–3 MeV secondary particles visible in Fig. 5(a) is caused by the β^- decay of ^{28}Al.

[3] The contribution of the secondary electrons to the PE-covered MOSFET spectrum will be effectively removed by the subtraction of the bare MOSFET signal.

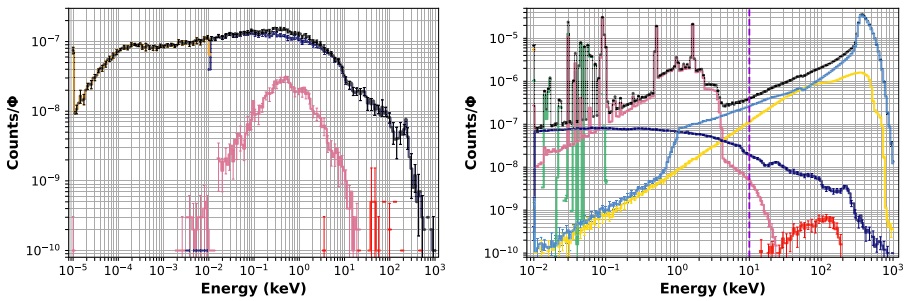

(a) Deposited energy, bare MOSFET (b) Deposited energy, 1 μm B_4C

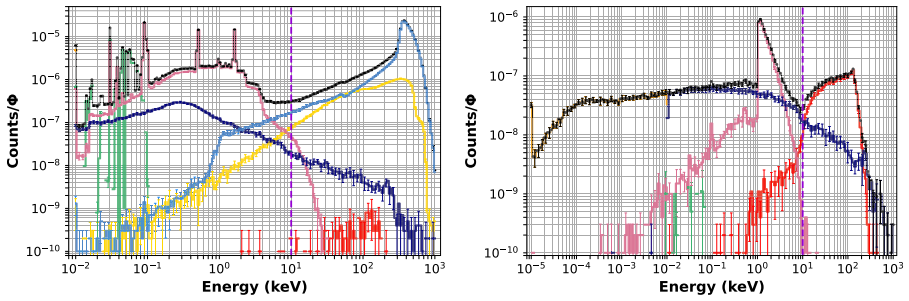

(c) Deposited energy, 1 mm Cd and 1 μm B_4C (d) Deposited energy, 5 mm PE

Fig. 4. Energy spectra (in units of particle flux density vs. energy) of secondary particle species depositing energy in the sensitive volume of the bare MOSFET 4(a), MOSFET covered with 1 μm B_4C 4(b), 1 mm Cd and 1 μm B_4C 4(c), and 5 mm PE 4(d). The total deposited energy (cumulative spectrum) is shown in black, α particles in blue, ^{7}Li ions in yellow, γ in green, electrons in pink, neutrons in orange, protons in red and other secondary particles in navy. Purple vertical dashed line denotes the spectral selectivity thresholds. This is omitted in 4(a) since the detector is sensitive to γ and other secondary particles generated within the SV.

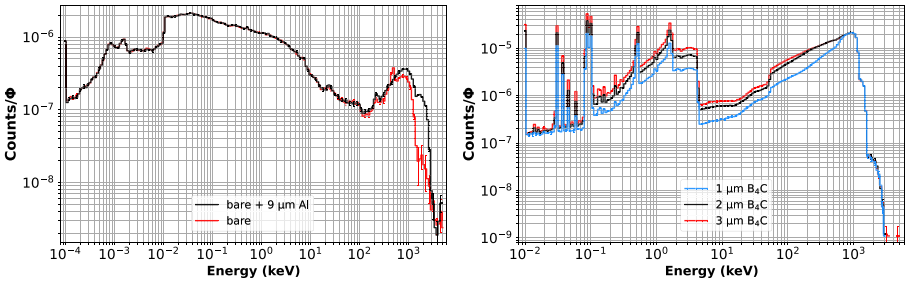

(a) Kinetic energy, bare MOSFET (b) Kinetic energy, B_4C

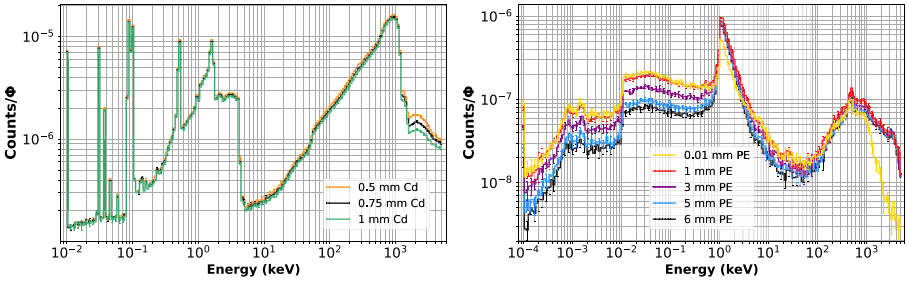

(c) Kinetic energy, Cd + 1 μm B_4C (d) Kinetic energy, PE

Fig. 5. Kinetic energy spectra of secondary particles entering the sensitive volume of the bare MOSFET detector with and without the 9 μm Al layer 5(a) and MOSFETs covered with 1 μm, 2 μm and 3 μm B_4C converter 5(b); 0.5 mm, 0.75 mm and 1 mm Cd filter and 1 μm B_4C converter 5(c) and 0.01 mm, 1 mm, 3 mm, 5 mm and 6 mm PE converter 5(d), irradiated in air.

The probability of neutron capture reactions is the lowest for the thinnest (1 μm) B_4C converter. This decreases the α and ^{7}Li production yields, but minimises the generation of γ-rays compared to thicker converters. Moreover, the high LET α and ^{7}Li particles lose smaller fractions of their kinetic energy within a thinner converter layer; the 1 μm converter allows approximately 75% of the α particles to reach the SV, versus 68% and 65% for 2 μm and 3 μm B_4C layer, respectively, due to smaller energy losses. This results in the sharp peak at 300–400 keV which is visible in Fig. 6(b). These results are in agreement with Höglund et al. (2012), a manufacturer of the B_4C converters, who

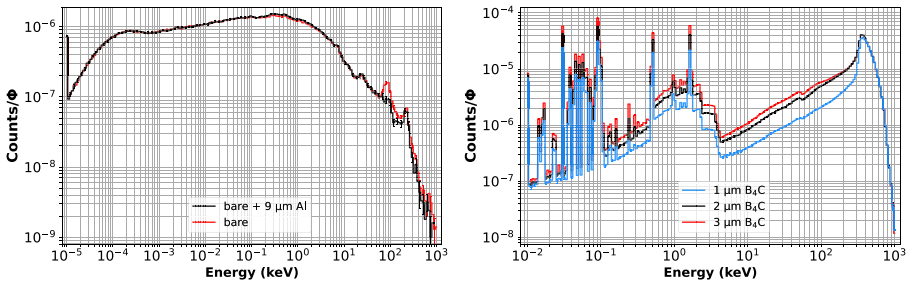

(a) Deposited energy, bare MOSFET (b) Deposited energy, B_4C

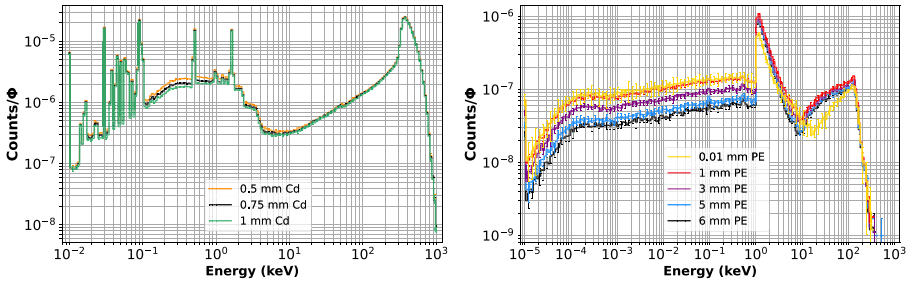

(c) Deposited energy, Cd + 1 μm B_4C (d) Deposited energy, PE

Fig. 6. Energy spectra of secondary particles depositing energy in the sensitive volume of the bare MOSFET detector with and without the 9 μm Al layer 6(a) and MOSFETs covered with 1 μm, 2 μm and 3 μm B_4C converter 6(b); 0.5 mm, 0.75 mm and 1 mm Cd filter and 1 μm B_4C converter 6(c) and 0.01 mm, 1 mm, 3 mm, 5 mm and 6 mm PE converter 6(d), irradiated in air.

Table 3
Calculated doses (per primary particle in the beam) deposited in the SV of four MOSFET detectors irradiated in air.

Dose (Gy/n)	MOSFET + 1 μm B_4C	MOSFET + 1 mm Cd & 1 μm B_4C	MOSFET + 5 mm PE	Bare MOSFET + 9 μm Al
D_{total}	$(1.879 \pm 0.002) \times 10^{-10}$	$(1.229 \pm 0.002) \times 10^{-10}$	$(2.493 \pm 0.017) \times 10^{-13}$	$(4.197 \pm 0.118) \times 10^{-14}$
$D_{^{10}B(n,\alpha)^7Li}$	**$(1.726 \pm 0.002) \times 10^{-10}$**	**$(1.128 \pm 0.001) \times 10^{-10}$**	N/A	N/A
$D_{^{10}B(n,\gamma)^7Li}$	$(1.486 \pm 0.126) \times 10^{-18}$	$(9.635 \pm 1.613) \times 10^{-19}$	N/A	N/A
$D_{^7Li}$	$(1.507 \pm 0.006) \times 10^{-11}$	$(9.894 \pm 0.031) \times 10^{-12}$	N/A	N/A
$D_{^1H(n,\gamma)^1H}$	–	–	–	–
$D_{^1H(n,p)^1H}$	$(1.904 \pm 0.382) \times 10^{-15}$	$(1.905 \pm 0.128) \times 10^{-15}$	**$(2.057 \pm 0.010) \times 10^{-13}$**	–
$D_{^{14}N(n,p)^{14}C}$	$(1.039 \pm 0.750) \times 10^{-16}$	$(9.409 \pm 3.081) \times 10^{-17}$	–	$(1.905 \pm 1.177) \times 10^{-16}$
D_{other}	$(2.304 \pm 0.154\times 10^{-13}$	$(2.313 \pm 0.019\times 10^{-13}$	$(4.357 \pm 0.137) \times 10^{-14}$	$(4.179 \pm 0.120) \times 10^{-14}$
D_{est}	$(1.878 \pm 0.002) \times 10^{-10}$	$(1.228 \pm 0.002) \times 10^{-10}$	$(2.072 \pm 0.139) \times 10^{-13}$	N/A

reported a maximum α particle escape efficiency from 1 μm B_4C of around 71% for a monoenergetic beam of 2.75 keV incident neutrons. No differences were observed for ^{7}Li ions; in all three cases, the percentage of alpha particles that cross the sensitive volume remains at 6%. The energy deposited in the SV is 3 to 4 orders of magnitude larger than that deposited in the bare MOSFET, thereby the subtraction of this dose does not significantly alter the result. The spectral selectivity ratio is thus maximised for the thinnest converter layer (1 μm). The optimal cadmium thickness was found be 1 mm, which provided the lowest SSR. No significant differences were observed between the three evaluated cadmium thicknesses in either the neutron kinetic energy or the energy deposition spectra; this is because the contribution of the thermal neutron component is around 4% of the total. Another factor we considered during the selection of the thickness of cadmium is the transmission of thermal neutrons reported in the literature, which is around 1% for 1 mm of cadmium (with transmission increasing as the cadmium thickness decreases) (D'Mellow et al., 2007; Volknandt et al., 2020).

While the 0.2 mm PE converter maximises the energy deposited in the SV resulting from the ^{1}H(n, p)^{1}H reaction and the 6 mm PE converter provides the best spectral selectivity ratio, the 5 mm PE converter achieves the best estimate of the corrected energy deposition corresponding the band of interest (with only a slightly reduced spectral selectivity compared to the 6 mm converter).

3.2. Response characterisation of the optimised MOSFET detectors

Tables 3 and 4 list the calculated doses corresponding to secondary particles entering the SV of the optimised MOSFET detectors in the air and on the surface of the water phantom, respectively. The highlighted fields relate to the signals from the radiation field components that the MOSFET detectors are designed to measure (i.e., the dose components resulting from the reactions which are maximally sensitive to thermal and epithermal, epithermal and fast neutron spectral components).

The results demonstrate that the energy deposited in the SV of the B_4C-covered (and Cd + B_4C) MOSFET is mainly due to the α and ^{7}Li particles, while recoil protons from the ^{1}H(n,p)^{1}H reaction constitute the majority of the dose in the MOSFET covered with a 5 mm PE layer. Due to the low LET of γ radiation and the SV thickness of only 1 μm, the response of the MOSFETs to either ^{10}B(n, γ)^{7}Li or ^{1}H(n, γ)^{2}H is negligible. The bare MOSFET detector is mainly sensitive to the γ radiation and particles generated within the SV of the detector. The estimated dose value (D_{est}) obtained from the B_4C- and Cd+B_4C-covered MOSFET following irradiation while placed on the surface of the water phantom increases by 74% and 117% relative to its response when irradiated in air, respectively. By contrast, the estimated dose value obtained from the PE-covered MOSFET decreases by 9.5% relative to air. The B_4C-covered MOSFET sees a significant increase

Table 4
Calculated doses deposited in the SV of four MOSFET detectors placed on the surface of the water phantom.

Dose (Gy/n)	MOSFET + 1 μm B_4C	MOSFET + 1 mm Cd & 1 μm B_4C	MOSFET + 5 mm PE	Bare MOSFET + 9 μm Al
D_{total}	$(3.27 \pm 0.02) \times 10^{-10}$	$(2.60 \pm 0.03) \times 10^{-10}$	$(2.50 \pm 0.20) \times 10^{-13}$	$(5.36 \pm 0.94) \times 10^{-14}$
$D_{^{10}B(n,\alpha)^7Li}$	**$(3.00 \pm 0.02) \times 10^{-10}$**	**$(2.38 \pm 0.02) \times 10^{-10}$**	N/A	N/A
$D_{^{10}B(n,\gamma)^7Li}$	$(4.62 \pm 3.21) \times 10^{-18}$	$(4.02 \pm 1.72) \times 10^{-18}$	N/A	N/A
$D_{^7Li}$	$(2.59 \pm 0.08) \times 10^{-11}$	$(2.15 \pm 0.09) \times 10^{-11}$	N/A	N/A
$D_{^1H(n,\gamma)^1H}$		–	–	–
$D_{^1H(n,p)^1H}$	$(1.02 \pm 0.17) \times 10^{-14}$	$(9.13 \pm 4.87) \times 10^{-15}$	**$(1.89 \pm 0.19) \times 10^{-13}$**	–
$D_{^{14}N(n,p)^{14}C}$	$(7.51 \pm 0.42) \times 10^{-15}$	–	–	–
D_{other}	$(3.85 \pm 0.20) \times 10^{-13}$	$(5.55 \pm 0.16) \times 10^{-13}$	$(6.08 \pm 1.25) \times 10^{-14}$	$(5.31 \pm 0.92) \times 10^{-14}$
D_{est}	$(3.26 \pm 0.02) \times 10^{-10}$	$(2.60 \pm 0.03) \times 10^{-10}$	$(1.97 \pm 0.23) \times 10^{-13}$	N/A

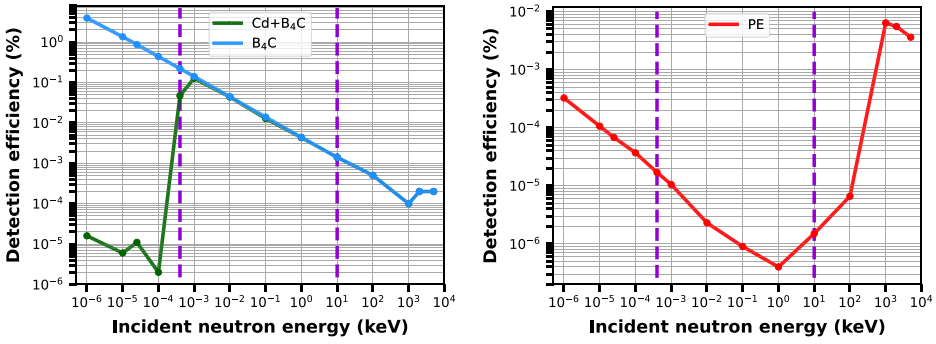

Fig. 7. Detection efficiency of the MOSFET detectors covered with a) 1 μm B_4C and 1 mm Cd + 1 μm B_4C, and b) 5 mm PE as a function of incident neutron energy. Purple vertical lines denote the epithermal (0.4 eV) and fast neutron (10 keV) energy thresholds.

in dose deposited since some of the neutrons from the periphery of the beam (primarily in the dominant epithermal spectral component) scatter backwards from the phantom and are captured in the converter. The decrease in D_{est} obtained from the PE-covered MOSFET is not a result of any modification to the fast neutron component of the beam, which is unchanged from the case in air, but rather due to a 27.4% increase in the backscattered dose received by the bare MOSFET compared to the dose obtained in air which is subtracted from the total dose of the PE-covered MOSFET.

The detection efficiency (ϵ) of MOSFET detectors covered with 1 μm B_4C, 1 mm Cd and 1 μm B_4C, and PE, as a function of incident neutron energy, is presented in Fig. 7. As the data acquisition (i.e., MOSFET readout system) has not been modelled in this work, ϵ can be considered essentially as a product of two factors: the cross-section of the reaction of interest (the main component of the deposited dose), and the probability of the reaction products reaching the SV (geometric constraint). This second factor is particularly important for the B_4C- and Cd + B_4C-coated MOSFETs since the α particles are emitted isotropically, and only a fraction of them will reach the SV. The simulated detection efficiency for the Tsukuba neutron spectrum was $(5.61 \pm 0.02) \times 10^{-2}$ % and $(2.23 \pm 0.11) \times 10^{-4}$ %, respectively. The $^{10}B(n, \alpha)^7Li$ reaction rate is approximately 250 times higher than that of $^1H(n,p)^1H$.

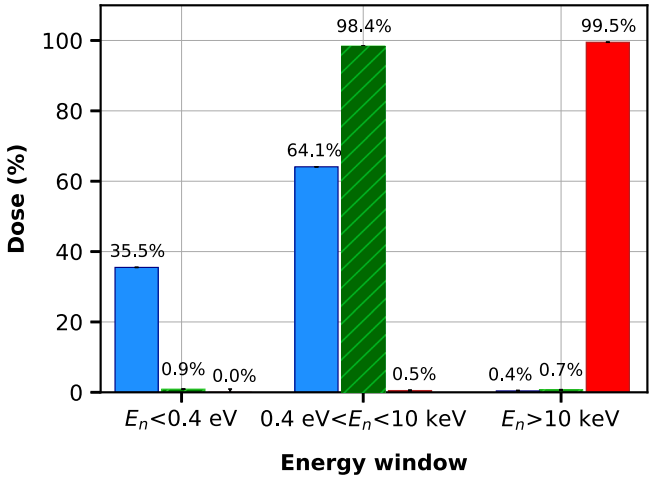

Fig. 8. Energy-specific sensitivity of MOSFET detectors covered with various converters to the iBNCT neutron spectrum (in air). B_4C-covered (blue): thermal and epithermal; Cd and B_4C-covered (green): epithermal; and PE-covered (red): fast. Each detector demonstrates high specificity to its targeted energy range.

3.3. Sensitivity of the MOSFET detectors to changes in the neutron fluence

Simulated normalised sensitivity of the MOSFET detectors to the thermal, epithermal and fast neutron regions of the University of Tsukuba Hospital neutron spectrum is shown in Fig. 8. Given that the fraction of thermal neutrons (E_n < 0.4 eV) constitutes fewer than 4% of the total simulated AB-BNCT neutron spectrum, yet it results in a 35% response from the MOSFET covered with B_4C, it can be inferred that the sensitivity of the B_4C-covered MOSFET rapidly increases with decreasing incident neutron energy. With the implementation of the 1 mm cadmium thermal neutron filter, more than 98% of the signal is generated by epithermal neutrons. On the other hand, almost the entire signal obtained from the simulated PE-covered MOSFET detector was indirectly caused by neutrons with energies above 10 keV.

The response of the quad-MOSFET device to changes in beam fluence is listed in Table 5. The total beam fluence was varied by ±10% relative to the nominal (Tsukuba) spectrum, corresponding to 10^9 n/cm^2 or 1 s of irradiation at a clinical neutron beamline. The changes in the ratio of thermal to epithermal and fast to epithermal neutron doses were calculated in each case. The estimated thermal and epithermal, epithermal and fast neutron doses change proportionally to beam fluence; however, their ratio remains the same. This demonstrates

Table 5
Impact of changes to the nominal neutron beam fluence (Φ_{nom}) on estimated dose deposited in each detector following irradiation in air, and the resulting ratio of the corrected thermal to epithermal ($\frac{(D_{B_4C-bare})-(D_{Cd,B_4C-bare})}{D_{Cd,B_4C-bare}}$) and fast to epithermal neutron dose ratios ($\frac{D_{PE-bare}}{D_{Cd,B_4C-bare}}$).

	Dose(Gy/n)				Ratio	
	B_4C	Cd + B_4C	PE	Bare	$\frac{D_{thermal}}{D_{epithermal}}$	$\frac{D_{fast}}{D_{epithermal}}$
Φ_{nom}	1.88×10^{-10}	1.23×10^{-10}	2.48×10^{-13}	4.49×10^{-14}	0.53 ± 0.02	(2.02 ± 0.04) $\times 10^{-3}$
$\Phi_{nom} \times 0.9$	1.69×10^{-10}	1.10×10^{-10}	2.24×10^{-13}	4.03×10^{-14}	0.53 ± 0.03	(2.03 ± 0.05) $\times 10^{-3}$
$\Phi_{nom} \times 1.1$	2.07×10^{-10}	1.35×10^{-10}	2.73×10^{-13}	4.99×10^{-14}	0.53 ± 0.03	(2.02 ± 0.03) $\times 10^{-3}$

the capability of the proposed device to monitor real-time beam flux fluctuations.

3.4. Summary and overall design recommendation

The optimal B_4C converter thickness was found to be 1 μm. While it is possible to directly coat the detector's surface with B_4C instead of using the aluminium support layer (Guardiola et al., 2013), this layer serves a useful function as a filter to block protons induced by neutron inelastic scattering on nitrogen $^{14}N(n,p)^{14}C$ in the air. An additional 1 mm cadmium layer is sufficient to filter out almost the entire thermal component from the signal.

The polyethylene converter cannot be too thin if it is to produce a sufficient reaction rate, nor can it be too thick since lower energy protons will be absorbed in polyethylene or will escape with energy too low to penetrate through the 1 μm aluminium gate contact layer on top of the SV (the mean range of 100 keV protons in aluminium is 0.84 μm). A PE converter thickness of 5 mm was found to provide the optimal fast neutron-to-proton conversion rate and spectral selectivity, allowing for an indirect measurement of neutrons from the very beginning of the fast neutron range. The recommended PE and aluminium layers' thickness is also sufficient to block the 0.56 MeV recoil protons (which have a mean range of approximately 10 μm in polyethylene).

The bare MOSFET detector is specifically designed to measure the γ component and other secondary particles generated within the SV that are used for the subtraction method to increase the overall measurement accuracy of the quad-MOSFET device. Ideally, this signal should not require a correction factor and should contribute equally to the signal measured with the PE-coated detector; the simulated dose to the MOSFET with B_4C converter was approximately three orders of magnitude higher. We observed that the modified bare MOSFET detector with the additional 9 μm aluminium layer achieved similar sensitivity to the "subtraction particles" to the PE converter. Therefore, after subtracting the bare MOSFET signal, we can obtain an accurate signal corresponding to fast neutron fluence.

As expected, D_{α}, $D_{^1H(n,p)^1H}$ and $D_{^1H(n,\gamma)^2H}$ constitute the primary dose in B_4C (and Cd + B_4C) and PE-coated MOSFET detectors and the bare detector, respectively. In a clinical scenario, the γ background is more substantial due to neutron interactions within the beam shaping assembly (BSA), which was not considered in this work.

The proposed configuration of the quad-MOSFET device is suitable for monitoring relative changes in the neutron energy distribution and fluence with high sensitivity. For MOSFETs with a 1 μm thick SV and 1 μm B_4C converter operated in passive mode, and a 5 mm PE converter in an active mode, expected doses during a 30-minute BNCT session are of the order of 1–100 Gy with a ΔV_{th} shift of approximately 1000 mV and 0.1 Gy with a $\Delta V_{th} \approx 30$ mV, respectively.

The signal from the MOSFET covered with B_4C converter is nearly three orders of magnitude higher than for the other devices. This is due to (1) the high reaction neutron capture cross-section of ^{10}B; (2) the high LET of the resulting α particles and ^7Li ions; (3) average particle travel distance, which is slightly longer than the thickness of the SV; (4) the kinetic energy of the secondary particles when entering the SV; and (5) backscattered radiation. The sensitivity of individual MOSFET detectors can be manipulated by adjusting the gate oxide thickness. Such modifications may enable the detection of fluctuations in neutron fluence and spectrum of less than 10%.

The impact of the backscattered neutrons on the resulting signal is strongly energy-dependent and it is important to calibrate the detectors for individual AB-BNCT systems. For instance, thermal neutrons are more likely to be captured in the B_4C layer and less likely to reach it when backscattered from the surface than neutrons within the broad epithermal window. During treatment, the backscatter effect will vary depending on the area of the patient, i.e., the concentration of ^{10}B in the cells or scattering properties of anatomical structures such as bone. For the reference neutron spectrum used in this work, the contribution of the thermal component is approximately 4% and 80% for the epithermal energies. However, the dose increase due to backscattering in the thermal and epithermal neutron windows was predicted to be around 56% and 78%, respectively. Therefore, correction factors should be implemented to avoid over- or underestimating signals.

The proposed MOSFET detector/converter configurations are able to effectively estimate the relative thermal, epithermal and fast components of the total neutron flux as well as the γ background. These values can be used to calculate all four of the IAEA's figures of merit: firstly, (1) γ dose rate per unit of epithermal neutron flux; and (2) fast neutron dose rate per unit of epithermal neutron flux; next, since the neutron current is known, (3) its ratio to the epithermal neutron flux can also be obtained; and finally, (4) the thermal to epithermal neutron flux ratio can be calculated. However, the IAEA's guidelines were derived from gold activation foil measurements. In this work, we used reactions induced in ^{10}B, which has a different cross-sections to gold, notably being more sensitive to thermal neutrons. Therefore, the quad-MOSFET device should be calibrated for individual AB-BNCT systems, and equivalent relative ratios shall be measured to calculate the IAEA's FOMs.

4. Conclusion

In this work, we demonstrated that MOSFET detectors covered with 1 μm B_4C, 1 μm B_4C and 1 mm Cd, and 5 mm PE converters enable the measurement of the thermal, epithermal and fast neutron fluence via the $^{10}B(n, \alpha)^7Li$ reaction in B_4C, Cd-covered B_4C and $^1H(n,p)^1H$ in PE layers, respectively. A fourth MOSFET covered with a 9 μm aluminium layer provides information about γ contamination and secondary particles directly interacting with MOSFET that can be subtracted from the PE converter to increase overall accuracy. The impact of the aluminium on top of the B_4C (and Cd + B_4C) converter is negligible, and it is recommended to use a 9 μm aluminium layer on top of a bare MOSFET detector to block recoil protons resulting from neutron–nitrogen interactions in air.

The proposed combination of four MOSFET detectors is sensitive to small changes in the neutron spectrum. The simulated thermal to epithermal and fast to epithermal neutron ratios in the air, after subtracting the bare MOSFET detector signal, using the University of Tsukuba Hospital neutron spectrum, were around 0.5 and 2.0×10^{-3}. The sensitivity could be further improved if necessary by adjusting the gate oxide thickness.

The proposed quad-MOSFET device has been evaluated as a potential quality control device for real-time monitoring of incident beam quality in AB-BNCT, both in air and on the patient's surface. The device can be used for real-time beam monitoring in air, or to create a permanent record of the total fluence (measured in air). We do not

recommend using the device on the patient's surface, since the intensity of the backscattered radiation is considerable and differs for each detector configuration. It will also depend on the underlying anatomical structures that have varying scattering properties.

CRediT authorship contribution statement

Klaudiusz Jakubowski: Writing – original draft, Visualization, Validation, Software, Project administration, Methodology, Investigation, Funding acquisition, Formal analysis, Data curation, Conceptualization. **James Vohradsky:** Writing – review & editing, Software, Methodology, Investigation. **Andrew Chacon:** Writing – review & editing, Methodology. **Daniel R. Franklin:** Writing – review & editing, Methodology. **Linh T. Tran:** Writing – review & editing, Supervision, Methodology, Investigation. **Susanna Guatelli:** Writing – review & editing, Supervision, Software, Methodology, Investigation. **Mitra Safavi-Naeini:** Writing – review & editing, Visualization, Validation, Supervision, Resources, Methodology, Investigation, Formal analysis, Data curation, Conceptualization. **Anatoly Rosenfeld:** Writing – review & editing, Visualization, Validation, Supervision, Resources, Project administration, Methodology, Investigation, Funding acquisition, Formal analysis, Conceptualization.

Declaration of competing interest

The authors declare that they have no known competing financial interests or personal relationships that could have appeared to influence the work reported in this paper.

Data availability

Data will be made available on request.

Acknowledgements

This research was undertaken with the support of Tesla high-performance computing cluster at ANSTO, Australia and by the Australian Government's National Collaborative Research Infrastructure Strategy (NCRIS), with access to computational resources provided by the Gadi through the National Computational Merit Allocation Scheme. The authors wish to acknowledge the support of the University of Wollongong Matching Scholarship and the International Postgraduate Tuition Award, and the Australian Institute of Nuclear Science and Engineering (AINSE) Residential Student Scholarship (RSS).

Appendix A. Supplementary data

Supplementary material related to this article can be found online at https://doi.org/10.1016/j.radmeas.2024.107253.

References

Agostinelli, S., Allison, J., Amako, et al., 2003. Geant4—a simulation toolkit. Nucl. Instrum. Methods Phys. Res. A (ISSN: 0168-9002) 506 (3), 250–303. http://dx.doi.org/10.1016/s0168-9002(03)01368-8.

Allison, J., Amako, K., Apostolakis, et al., 2006. Geant4 developments and applications. IEEE Trans. Nucl. Sci. (ISSN: 0018-9499) 53 (1), 270–278. http://dx.doi.org/10.1109/tns.2006.869826.

Allison, J., Amako, K., Apostolakis, J., et al., 2016. Recent developments in geant4. Nucl. Instrum. Methods Phys. Res. A 835, 186–225. http://dx.doi.org/10.1016/j.nima.2016.06.125.

Ambrozova, I., Davidkova, M., Brabcova, K.P., et al., 2017. Contribution of different particles measured with track etched detectors onboard ISS. Radiat. Prot. Dosim. http://dx.doi.org/10.1093/rpd/ncx189.

Barth, R.F., Zhang, Z., Liu, T., 2018. A realistic appraisal of boron neutron capture therapy as a cancer treatment modality. Cancer Commun. 38 (1), 36. http://dx.doi.org/10.1186/s40880-018-0280-5.

Costa, A.M., Barbi, G.L., Bertucci, E.C., et al., 2010. In vivo dosimetry with thermoluminescent dosimeters in external photon beam radiotherapy. Appl. Radiat. Isot. 68 (4–5), 760–762. http://dx.doi.org/10.1016/j.apradiso.2009.09.039.

de Prez, L., Woodings, S., de Pooter, J., et al., 2019. Direct measurement of ion chamber correction factors, k q and k b, in a 7 mv mri-linac. Phys. Med. Biol. 64 (10), 105025. http://dx.doi.org/10.1088/1361-6560/ab1511.

Devic, S., Aldelaijan, S., Bekerat, H., 2019. Impact of inertia on possible fundamental drawbacks in radiochromic film dosimetry. Phys. Medica 66, 133–134. http://dx.doi.org/10.1016/j.ejmp.2019.08.019.

D'Mellow, B., Thomas, D.J., Joyce, M.J., et al., 2007. The replacement of cadmium as a thermal neutron filter. Nucl. Instrum. Methods Phys. Res. A (ISSN: 0168-9002) 577 (3), 690–695. http://dx.doi.org/10.1016/j.nima.2007.05.001.

Dymova, M.A., Taskaev, S.Y., Richter, V.A., Kuligina, E.V., 2020. Boron neutron capture therapy: Current status and future perspectives. Cancer Commun. 40 (9), 406–421. http://dx.doi.org/10.1002/cac2.12089.

Fragopoulou, M., Konstantakos, V., Zamani, M., et al., 2010. High sensitivity MOSFET-based neutron dosimetry. Nucl. Instrum. Methods Phys. Res. A 621 (1–3), 611–614. http://dx.doi.org/10.1016/j.nima.2010.06.095.

Futamura, G., Kawabata, S., Nonoguchi, N., et al., 2017. Evaluation of a novel sodium borocaptate-containing unnatural amino acid as a boron delivery agent for neutron capture therapy of the f98 rat glioma. Radiat. Oncol. 12 (1), http://dx.doi.org/10.1186/s13014-017-0765-4.

García, A., Mendoza, E., Cano-Ott, D., 2013. Validation of the thermal neutron physics in geant4. In: G4 Hadronic Group Meeting. 17 2013, CERN, Geneva Switzerland.

Guardiola, C., Gómez, F., Fleta, C., et al., 2013. Neutron measurements with ultra-thin 3d silicon sensors in a radiotherapy treatment room using a siemens PRIMUS linac. Phys. Med. Biol. 58 (10), 3227–3242. http://dx.doi.org/10.1088/0031-9155/58/10/3227.

Hartling, K., Ciungu, B., Li, G., et al., 2018. The effects of nuclear data library processing on geant4 and mcnp simulations of the thermal neutron scattering law. Nucl. Instrum. Methods Phys. Res. A (ISSN: 0168-9002) 891, 25–31. http://dx.doi.org/10.1016/j.nima.2018.02.053.

Höglund, C., Birch, J., Andersen, K., et al., 2012. B4c thin films for neutron detection. J. Appl. Phys. 111 (10), 104908. http://dx.doi.org/10.1063/1.4718573.

Hu, N., Tanaka, H., Kakino, R., et al., 2021. Evaluation of a treatment planning system developed for clinical boron neutron capture therapy and validation against an independent monte carlo dose calculation system. Radiat. Oncol. (ISSN: 1748-717X) 16 (1), http://dx.doi.org/10.1186/s13014-021-01968-2.

IAEA, 2001. Current status of neutron capture therapy. In: Number 1223 in TECDOC Series. International Atomic Energy Agency, Vienna, URL https://www.iaea.org/publications/6168/current-status-of-neutron-capture-therapy.

ISNCT, 2022. Accelerator-based BNCT projects. Website, URL https://isnct.net/bnct-boron-neutron-capture-therapy/accelerator-based-bnct-projects-2021/. (Accessed 23 December 2023).

Jakubowski, K., Chacon, A., Tran, L.T., et al., 2023. A monte carlo model of the dingo thermal neutron imaging beamline. Sci. Rep. 13 (1), http://dx.doi.org/10.1038/s41598-023-44035-4.

Jong, W.L., Wong, J.H.D., Ung, N.M., et al., 2014. Characterization of moskin detector for in vivo skin dose measurement during megavoltage radiotherapy. J. Appl. Clin. Med. Phys. 15 (5), 120–132. http://dx.doi.org/10.1120/jacmp.v15i5.4869.

Kaplan, G.I., Rosenfeld, A.B., Allen, B.J., et al., 1999. Fission converter and metal–oxide–semiconductor field effect transistor study of thermal neutron flux distribution in an epithermal neutron therapy beam. Med. Phys. 26 (9), 1989–1994. http://dx.doi.org/10.1118/1.598703.

Kiyanagi, Y., Sakurai, Y., Kumada, H., Tanaka, H., 2019. Status of Accelerator-Based BNCT Projects Worldwide. AIP Publishing, 050012. http://dx.doi.org/10.1063/1.5127704.

Kumada, H., Naito, F., Hasegawa, K., et al., 2018. Development of LINAC-based neutron source for boron neutron capture therapy in university of Tsukuba. Plasma Fusion Res. 13, http://dx.doi.org/10.1585/pfr.13.2406006.

Kweon, D.C., Lee, J.-S., Goo, E.-H., et al., 2011. An overall stem effect, including stem leakage and stem scatter, for a TM30013 farmer-type chamber. J. Korean Phys. Soc. 58 (6), 1688–1696. http://dx.doi.org/10.3938/jkps.58.1688.

Lamrabet, A., Maghnouj, A., Tajmouati, J., Bencheikh, M., 2021. Geant4 characterization of the neutronic behavior of the active zone of the megapie spallation target. Nucl. Eng. Technol. (ISSN: 1738-5733) 53 (10), 3164–3170. http://dx.doi.org/10.1016/j.net.2021.05.002.

Malouff, T.D., Seneviratne, D.S., Ebner, D.K., et al., 2021. Boron neutron capture therapy: A review of clinical applications. Front. Oncol. 11, http://dx.doi.org/10.3389/fonc.2021.601820.

Ogawara, R., Kusumoto, T., Konishi, T., et al., 2020. Detection of alpha and ^{7}Li particles from ^{10}B(n, α)^{7}Li reactions using a combination of CR-39 nuclear track detector and potassium hydroxide-ethanol-water solution in accelerator-based neutron fields. Nucl. Instrum. Methods Phys. Res. B http://dx.doi.org/10.1016/j.nimb.2020.01.030.

Olko, P., 2010. Advantages and disadvantages of luminescence dosimetry. Radiat. Meas. 45 (3–6), 506–511. http://dx.doi.org/10.1016/j.radmeas.2010.01.016.

Rosenfeld, A.B., Kron, T., d'Errico, F., Moscovitch, M., 2011. Advanced semiconductor dosimetry in radiation therapy. In: AIP Conference Proceedings. AIP, pp. 48–74. http://dx.doi.org/10.1063/1.3576159.

Santos, T., Ventura, T., do Carmo Lopes, M., 2021. A review on radiochromic film dosimetry for dose verification in high energy photon beams. Radiat. Phys. Chem. 179, 109217. http://dx.doi.org/10.1016/j.radphyschem.2020.109217.

Suzuki, M., 2019. Boron neutron capture therapy (BNCT): a unique role in radiotherapy with a view to entering the accelerator-based BNCT era. Int. J. Clin. Oncol. 25 (1), 43–50. http://dx.doi.org/10.1007/s10147-019-01480-4.

Takada, M., Nunomiya, T., Masuda, A., et al., 2021. Development of a real-time neutron beam detector for boron neutron capture therapy using a thin silicon sensor. Appl. Radiat. Isot. 176, 109856. http://dx.doi.org/10.1016/j.apradiso.2021.109856.

Tanaka, H., Takata, T., Sakurai, Y., et al., 2018. Development of real-time thermal neutron monitor array for boron neutron capture therapy. Ther. Radiol. Oncol. (ISSN: 2616-2768) 2, 51. http://dx.doi.org/10.21037/tro.2018.10.10.

Thulliez, L., Jouanne, C., Dumonteil, E., 2022. Improvement of geant4 neutron-hp package: From methodology to evaluated nuclear data library. Nucl. Instrum. Methods Phys. Res. A (ISSN: 0168-9002) 1027, 166187. http://dx.doi.org/10.1016/j.nima.2021.166187.

van der Ende, B., Atanackovic, J., Erlandson, A., Bentoumi, G., 2016. Use of geant4 vs. mcnpx for the characterization of a boron-lined neutron detector. Nucl. Instrum. Methods Phys. Res. A (ISSN: 0168-9002) 820, 40–47. http://dx.doi.org/10.1016/j.nima.2016.02.082.

Vohradsky, J., Guatelli, S., Davis, J.A., et al., 2019. Evaluation of silicon based microdosimetry for boron neutron capture therapy quality assurance. Phys. Medica 66, 8–14. http://dx.doi.org/10.1016/j.ejmp.2019.09.072.

Vohradsky, J., Tran, L.T., Guatelli, S., et al., 2021. Response of soi microdosimeter in fast neutron beams: experiment and monte carlo simulations. Phys. Medica (ISSN: 1120-1797) 90, 176–187. http://dx.doi.org/10.1016/j.ejmp.2021.09.008.

Volknandt, M., Eberhardt, K., Endres, A., et al., 2020. Neutron capture cross section for 10be. J. Phys. Conf. Ser. (ISSN: 1742-6596) 1668, 012048. http://dx.doi.org/10.1088/1742-6596/1668/1/012048.